Resolving Topographic Steady-State in Taiwan

Drew Bradley Stolar

A thesis submitted in partial fulfillment
of the requirements for the degree of

Master of Science

University of Washington

2003

Program Authorized to Offer Degree: Earth and Space Sciences

University of Washington

Graduate School

This is to certify that I have examined this copy of a master's thesis by

Drew Bradley Stolar

and have found that it is complete and satisfactory in all respects,
and that any and all revisions required by the final
examining committee have been made.

Committee Members:

_____

Dr. Sean D. Willett

_____

Dr. David R. Montgomery

Date: _____

In presenting this thesis in partial fulfillment of the requirements for a Master's degree at the University of Washington, I agree that the Library shall make its copies freely available for inspection. I further agree that extensive copying of this thesis is allowable only for scholarly purposes, consistent with "fair use" as prescribed in the U.S. Copyright Law. Any other reproduction for any purpose or by any means shall not be allowed without my written permission.

Signature 

Date 6/6/13

University of Washington

Abstract

Resolving Topographic Steady-State in Taiwan

by Drew Bradley Stolar

Chair of Supervisory Committee:

Associate Professor Dr. Sean D. Willett
Department of Earth and Space Sciences

The arc-continent collision in Taiwan has resulted in surface uplift, high relief, and high rates of erosion. Furthermore, because the collision is older in the north and propagates southward, Taiwan provides an opportunity to observe the evolution of topography, measure rates of evolution, test whether topographic steady-state (SS) is achieved, and, if SS does exist, to determine the magnitude and variability of the SS. I address these questions by analyzing a 40 m digital elevation (DEM) model of Taiwan at three scales of progressively higher resolution: cross-island swaths, drainage basins, and river profiles. The cross-sectional form of Taiwan, as measured by the volume, mean elevation, and maximum elevation within the cross-island swaths, grows northward from the southern tip of the island to 125 km north, where it reaches a constant size. This growth to a constant form is interpreted as a transition from pre-SS to SS topography. Assuming a range of collision propagation rates (55-90 mm/yr), the time to SS is 1.4-2.3 Myr after emergence above sea level. This transition also coincides with changes in the hypsometric curve and mean local slope of eastern Central Range drainage basins. However, in both cases, interpretations of these trends is not completely unambiguous, such that recognition of SS based solely on these analyses would be difficult. The Hack's Law exponent and the form of eastern Central Range

river profiles do not record the pre-SS to SS transition inferred from the swath profile data. The cross-sectional volume and mean elevation show a long wavelength (100 km) oscillation from 125 to 275 km north of the southern tip of the island with an amplitude of 16-20% of the steady values, respectively. In the north, this can be attributed to the Hsüehshan Range, which is a large-scale pop-up structure. Significant variability at each scale of analysis would preclude the recognition of topographic SS from a smaller-scale study.

TABLE OF CONTENTS

LIST OF FIGURES

ACKNOWLEDGMENTS

I would like thank my thesis committee members Sean Willett and Dave Montgomery for their help throughout this project. This work originated in a graduate seminar led by Sean and Dave. Preliminary analyses were done by Greg Balco, Chris Fuller, Karen Gran, Sara Mitchell, Chris Brummer, and Eliza Nemser. Thanks to my labmates Chris Fuller and Hans Schwaiger for their support, Noah Finnegan for discussing knickpoints, and to Leslie Hsu, Alison Anders, and Jon Tomkin for reading earlier versions of this thesis.

Chapter 1

INTRODUCTION

Geomorphologists have long recognized that equilibrium landforms represent a balance between surface processes, external forcing, and local conditions (Gilbert, 1877). Some workers have extended this concept to argue that entire mountain ranges are in topographic steady-state (SS), an equilibrium at which rates of rock uplift equal rates of erosion and surface uplift is zero (Penck, 1953; Suppe, 1981; Adams, 1980; Brandon et al., 1998; Kooi and Beaumont, 1996). Understanding SS mountain ranges is important because they provide both a baseline against which to compare other non-SS orogens (e.g., growing or decaying) and a testing ground in which to investigate theory and the processes that erode topography.

In a landscape with steady tectonic and erosional forcing, topographic SS is a natural consequence of the strong negative feedback between high local relief, as promoted by tectonic uplift, and high rates of erosion by slope-dependent surface processes (Ahnert 1970; Willett and Brandon, 2002). While the strictest definition of topographic SS requires static topography at all scales (Willett et al., 2001; Koons, 1989), most inferences of SS mountain ranges are derived from an observed balance between rock uplift and erosion rates. These observations, however, do not constrain the steadiness of topographic characteristics. How to recognize topographic SS by topographic analysis and how variable a morphology to expect in such landscapes remain unresolved issues.

Taiwan is an excellent natural laboratory to study these issues because of two factors: (i) the existence of conditions that encourage evolution of topography to

a SS and (ii) a tectonic setting that provides the opportunity to examine the time-evolution of topography. First, Taiwan is located in the subtropical Typhoon belt and receives heavy monsoonal rains and frequent typhoons. Mean annual precipitation in mountainous regions can exceed 6 m. These high precipitation rates drive rapid erosion ($\sim$5 mm/yr), which creates a steep and deeply incised landscape. Second, obliquity in the collision between the Eurasian continental margin and the Luzon Arc has resulted in the southward propagation of the collision over time (Suppe, 1981). Thus, the collision has been occurring in the north since the early Pliocene and is much younger in southern Taiwan. Using this space-time equivalence, I examine three principle questions: (1) How is topographic SS resolved by the topography of Taiwan? (2) What are the morphometric indices that are useful in identifying SS? (3) What is the expected variability in the morphology of a SS landscape?

I address these questions by analyzing a 40 m digital elevation model (DEM) of Taiwan with the standard geographic information system (GIS) techniques of the Arc/Info software package. Modules within Arc/Info can perform rapid mathematical operations on digital topography (e.g., calculation of gradients and areal distributions), automatically delineate of geomorphic features such as drainage basins and river profiles, and integrate paper-based map information, allowing one to do the analyses outlined above.

Chapter 2

STUDY AREA

Regional tectonic setting of Taiwan

The growth and destruction of the Taiwan accretionary wedge are direct results of the tectonic setting of the island. Taiwan lies along the subduction boundary between the Eurasian Plate and the Philippine Sea Plate (Fig. 2.1). Convergence between the two plates occurs at a rate of 70-82 mm/yr (Steno et al., 1977; Yu et al., 1997) and has an orientation of 35^o north of due west. The geodetic study of Yu et al. (1997) indicates that 50-60 mm/yr of shortening is accommodated by deformation in the Central Range.

Accretion of material from the continental shelf of the Eurasian plate into the Taiwan wedge has been driven by the collision between the Eurasian plate and the Luzon Arc (Suppe, 1981). For 200 km south of Taiwan, the Luzon Arc is oriented roughly north-south, such that the collision between the arc and the continental margin of the Eurasian plate is oblique. This obliquity has resulted in the southward propagation of the collision since its initiation at 5-7 Ma (Byrne and Liu, 2002). Therefore, there is a space-time equivalence that relates the age of the onset of the collision to the distance along the axis of the island (Fig. 2.1).

Suppe's original estimate (1981) of the propagation rate (90 mm/yr) was based on the assumption that the obliquity of the collision is best described by the angle between the Eurasian plate and the axis of the island. However, paleomagnetic data (Lee et al., 1991) demonstrate that the island has undergone clockwise rotation during collision. Byrne and Liu (2002) argue that the collision is better described by the angle between the continental margin and the Luzon Arc to the south, such that the

collision is less oblique. They estimate that the propagation rate is 55 mm/yr.

Steady propagation of the collision is not a universally accepted idea. Mouthereau et al. (2001) presented evidence that propagation in southern Taiwan is punctuated. They propose that thrusting related to the growth of the Taiwan wedge initiated at 5 Ma throughout southern Taiwan.

To the east of Taiwan is the Ryuku Trench, where the Philippine Sea plate subducts under the Eurasian plate (Fig. 2.1). North of the trench is the Okinawa Trough, which is a back-arc basin of the subduction system. Back-arc related extension, which is currently occurring onshore in the northeastern corner of the island (Yu et al., 1997) (Fig. 2.1), is believed to be an important contributor, along with erosion, to the destruction of the Taiwan wedge (Teng, 1996).

Tectonics and geology of Taiwan

The major tectonic domains of Taiwan are the onshore equivalents of extensive submarine features that are related to the collision of the continental margin of Eurasia and the Luzon Arc (Figs. 2.1 and 2.2). The Coastal Range, which is the northern extension of the Luzon Arc, is composed primarily of arc-related volcanics and olistostromal deposits (Teng, 1987). The Longitudinal Valley (LV) merges offshore with the Luzon Trough (Suppe, 1981) and has accommodated significant volumes of Miocene to present sediments, mainly from drainage basins in the eastern Central Range. Geodetic and creepmeter data indicate that the Coastal Range is being thrust over the LV at a rate of 17-30 mm/yr (Yu et al., 1997; Lee et al., 2001).

The Central Range (CR) consists of (i) the Backbone Range, which occupies the highest portions of the CR and is composed of Tertiary continental shelf sediments that have been metamorphosed into slates, and (ii) the pre-Tertiary basement, which is exposed exclusively within the eastern side of the CR and consists of greenschists, marbles, and gneisses. The CR is bounded in the northwest by the Lishan fault (Fig. 2.2), which separates it from the Hsüehshan Range. The Hsüehshan Range is a

crustal-scale pop-up structure composed of slates and metasandstones (Clark et al., 1993). To the west of the CR and Hsüehshan Range are the Western Foothills, where faulting and fold growth have repeatedly deformed Late Miocene-Pleistocene foreland basin sediments (Suppe, 1981).

I conduct analyses of swaths across the CR, Hsüehshan Range, and Western Foothills and of drainage basins in the eastern Central Range.

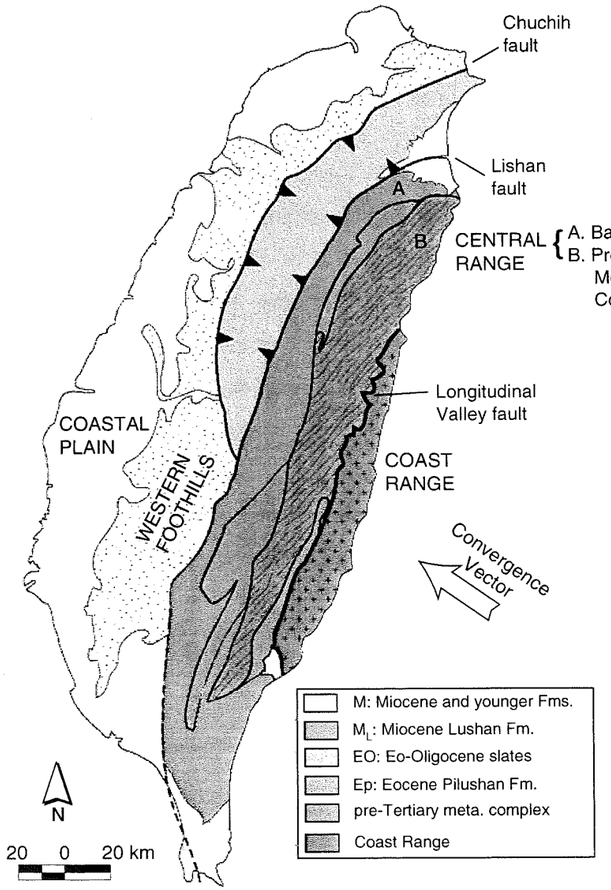

Figure 2.2: Tectonic and geologic domains of Taiwan with major faults.

Chapter 3

ANALYSIS

In order to characterize topography, I examine geomorphic properties at three spatial scales of progressively higher resolution: cross-island swaths, drainage basins, and river profiles. The intent of these analyses is to identify characteristics that define topographic SS and, if SS does exist, to determine the variability of the SS.

First, I construct swaths across the CR, Hsüehshan Range, and Western Foothills and calculate the volume, mean elevation, and maximum elevation within them. Second, I delineate drainage basins in the eastern Central Range and measure the distributions of elevation and topographic slope within each basin and the Hack's Law exponent. Third, I examine the form of river profiles in the ECR by documenting knickpoints and calculating profile concavities.

Swath profile analysis

Suppe (1981) analyzed large-scale characteristics of the Central Range–in particular, the range width and volume above sea level–and, based on the constancy of both quantities in the central CR, he concluded that part of the Central Range is in a topographic SS. I conduct a similar analysis to either confirm or refute his findings and to examine variability in the data he observed.

Within the *ArcEdit* module of *Arc/Info*, I construct a set of 5 km wide swaths that are oriented perpendicular to the island axis (Fig. 3.1b). The western coastal plain, LV, and Coastal Range are removed from the analysis by clipping the swaths to the eastern boundary of the Central Range and the western boundary of the Western Foothills (thick black line in Fig. 3.1b). Within this region, there are a total of

78 swaths. The swaths, which are defined as polygons within *ArcEdit*, are then transformed into a grid of points. The area per swath ranges from 20 km^2 in the northern and southern extremities to 500 km^2 in the middle of the island. Using the *Grid* module of *Arc/Info*, I calculate the volume above sea level, mean elevation, and maximum elevation of each swath. These values are then projected onto the transect A-A′ shown in Fig. 3.1b.

Along the transect (Fig. 3.2), the volume and mean and maximum elevation generally increase from the southern tip of the island to the southern end of the LV ~125-150 km to the north. North of this point, these quantities attain roughly constant values until, at 275 km N, they decrease rapidly to the northern tip of the island. From 125 km N the values increase to a maximum at 175 km N, which corresponds to the highest and widest portion of the Yushan Range (Fig. 3.1). The values then decrease to a minimum at 225 km N, which corresponds to an embayment in the western side of the Central Range centered around the city of Puli (Fig. 3.1). The values then increase to the north from 225 km N to 275 km N. This increase corresponds to the Hsüehshan Range, which has a maximum elevation similar to that of the Yushan Range. The amplitudes of the oscillation from 125 to 175 km N are 16%, 20%, and 8% of the average values of the volume, mean elevation, and maximum elevation, respectively.

Basin analysis

Basins in the eastern Central Range (ECR) are all oriented roughly perpendicular to the axis of the range. Accepting the space-time equivalence of the collision, the progression in inferred age is associated with distance of the basin outlet from the southern tip of the island. On the western side of the range, however, basin boundaries are often defined by NNE-SSW trending structures, particularly in the Western Foothills (Fig. 3.1). Therefore, the association of north-south position and inferred age is not clear in many cases. For these reasons, I limit the basin and profile analyses

to basins east of the main divide.

Drainage basins are delineated by a three-step process in the *Grid* module of *Arc/Info*. First, the direction of downstream flow is determined at all points. Second, the flow is routed downstream to calculate the contributing area of every point. Finally, drainage basins are defined as the upstream area that contributes to specific pour points, which are located at the intersection of the main channel of each basin with the boundary between the CR and LV.

River profiles are extracted using an AML script written by Harvey Greenberg. Profiles are defined as the upstream path with the smallest decrease in contributing area. This algorithm is able to negotiate past flat portions of the DEM. For each ECR basin, distance from the divide, elevation, and contributing area were recorded at every point along the main channel. Each profile originates at the basin outlet and extends to within 60 m of the drainage divide.

Hypsometry

The hypsometric curve is the normalized cumulative distribution function of elevation within a region. The form of the hypsometric curve has been used as both a measure of the maturity of a landscape (Strahler, 1964; Willgoose and Hancock, 1998) and as an indicator of the dominant erosive process (Brocklehurst and Whipple, 2001; Montgomery et al., 2002). Both Strahler (1964) and Willgoose and Hancock (1998) predict that pre-SS topography will have proportionately more area at higher elevations than SS topography. I calculate the hypsometric curves of the ECR basins because the form of the hypsometric curve is a potential an indicator of the state of topography.

The hypsometric curves can be segregated into two spatially correlated populations (Fig. 3.3). The transition between the two populations occurs between Basins 21 and 22, about 90 km north of the southern tip of the island. Basins 22-27 have more relative area at lower relative elevations than do Basins 1-21. The most significant outlier within the northern population, Basin 7, which is 230 km north of the southern tip, has a form more similar to that of the southern population.

To examine more subtle spatial correlation of hypsometry, each hypsometric curve is reduced to a single value, the hypsometric integral, by integrating with respect to area. In Fig. 3.4), the hypsometric integral is plotted against the position of the basin outlets along the transect A-A′ shown in Fig. 3.1. The distinction between the northern and southern populations is again noticeable, as is the similarity of Basin 7 to the southern basins. There is no apparent trend within the southern population such that the transition between the two populations is an abrupt increase of 0.08 between basins 22 and 21.

There is, however, a gradual trend in the entire hypsometric integral data set. The value of the hypsometric integral increases from 0.33±0.03 in the southernmost basins to 0.52 in Basin 17. This increase includes basins from the southern and northern populations. From Basin 17 to Basin 8, the value is relatively constant (0.48±0.05). North of Basin 7, the hypsometric integral decreases to ∼0.4 in the northernmost basins.

Basin slope distributions

Existence of topographic SS requires that hillslopes lower at the same rate as the channel network. Models of hillslope erosion differ in parameterization but most predict both a positive dependence of erosion rate on topographic slope and the existence of an upper threshold to the slope or relief that a hillslope can maintain (Burbank et al., 1996; Schmidt and Montgomery, 1995; Roering et al., 1999).

Montgomery and Brandon (2002) observed that long-term erosion rates in the Olympic Mountains are non-linearly dependent on local topographic slope. They found that the relationship was well described by the functional form of the non-linear hillslope diffusion law presented by Roering et al. (1999):

$$E \propto \frac{1}{1 - (\overline{S}/S_c)^2}, \tag{3.1}$$

where E is the erosion rate, $\overline{S}$ is the local slope averaged over a large area ($A > 10$ km^2), and S_c is a critical slope whose value is related to hillslope strength (Fig. 3.5).

As originally expressed by Roering et al. (1999), Eq. 3.1 related the material flux, rather than the erosion rate, to the topographic gradient for hillslopes with divergent drainage patterns. The functional form (Fig. 3.5), moreover, is particularly useful as a conceptual model because of its description of the positive slope–erosion rate relationship and its approximation of a threshold to hillslope gradient and relief. In general, Eq. 3.1 predicts that measures of slope should be able (i) to resolve variations in erosion rate in topography far from the critical slope and (ii) to resolve lithologic control of the critical slope S_c when topography is close to the threshold. Because demonstration of either prediction would be useful in resolving topographic SS, I analyze the distributions of local slope within the ECR basins.

Local slope is calculated at all points within a basin using the standard Arc/Info slope algorithm, which fits a 2^{nd} order polynomial to the eight surrounding cell elevations and calculates the magnitude of the steepest gradient of that surface. Slope distribution functions are then calculated for each basin. Because of the finite grid size, features less than 40 m are not resolved in the elevation field, and slope values in steep regions should be considered to be minimum estimates. To remove the contribution of alluvial valleys and alluvial fans, slopes lower than 5^o are not considered.

The slope distributions are generally Gaussian in form and usually have larger tails at lower slopes than at higher slopes. Because of the asymmetry in the tails, the distributions all fail the Kolmogorov-Smirnov test for normality at the 0.05 level (Press et al., 1998). This also causes some separation of the mean and mode of the distributions. The results of the following analysis of the means of the slope distributions, however, do not change if instead the medians or modes are considered.

In Fig. 3.6, I plot the mean and one standard deviation of each basin slope distribution versus transect distance. The data can be divided into four segments where: (i) mean basin slope increases from 23^o in Basin 27 to 31^o in Basin 20, (ii) slope is relatively constant ($31^o \pm 2^o$) from Basin 20 to Basin 10, (iii) slope increases from 33^o in Basin 9 to a maximum of 41^o in Basin 3, (iv) slope returns to $\sim 31^o$ in Basins 1 and 2. Within the region of constant mean slope, Basin 12 is the most significant

outlier, with a mean slope of 26°.

I examine the relationship between lithology and local slope by overlying the 1:500,000 geologic map of Ho (1986) on the DEM and computing the slope distribution for each major lithologic unit. The analysis is limited to the segment in which mean slope is relatively constant and to lithologic units with areas greater than 100 km^2.

The geologic map was scanned as four segments, digitized, referenced to the DEM, and then reassembled. Several factors, including few reference coordinates on the geologic map, sparse control points between the geologic map and DEM, and uncertainty about the original datum and projection of the geologic map all contribute to the significant mismatch between the geologic map and the DEM. Additionally, because of the difficulty of geologic mapping in the rugged, heavily forested ECR, there is considerable uncertainty in the mapped location of lithologic contacts (Wiltschkow, pers. comm. 2003). Where apparent, the mismatch varies in magnitude and orientation because (i) each map segment was referenced using a different set of control points and (ii) some manual adjustment of lithologic contacts was necessary to match adjacent segments. By comparing control points between the geologic map and the DEM, I estimate that features in the geologic map are within 2.5 km of their actual location in the DEM. Because the lithologic units cover more than 100 km^2, the effect of this mismatch on the slope distributions should be negligible.

The geology of the ECR is broadly characterized by two major groups: the Paleozoic-Mesozoic metamorphic basement and the lower-grade Tertiary metamorphic units (Fig. 3.7) (Ho, 1986). The general pattern of metamorphic grade is related to the duration of exhumation along the ECR; the highest grade unit of gneisses (PM1) occur exclusively in the northeastern corner of the ECR where exhumation has been occurring the longest, thus exhuming the pre-Tertiary metamorphic basement.

Basins with the highest mean slopes coincide with the exposures of the high-grade metamorphic units (Fig. 3.7). The mean slopes for the major lithologic units are shown in Fig. 3.8. The three highest-grade units, the PM1 gneisses, the PM2 marbles, and the PM3 greenschists have mean slopes of 32°-34° and the Tertiary

units (MI and Ep) and the lowest-grade unit of the basement group (PM4) have mean slopes of 29°-30°.

To determine how well the distribution of resistant lithologies describes the high mean slopes of basins in the north-east ECR, I plot the mean slope of Basins 1-20 versus the proportion of each basin within any of the three highest-grade lithologies (PM1, PM2, and PM3) (Fig. 3.9). In basins with greater than 75% of these lithologies, mean slope appears to be positively correlated to lithology, while in basins with less than 75%, there does not appear to be any correlation.

Hack's Law

Hack (1957) originally proposed a functional relationship between basin area A and outlet-to-divide stream length L:

$$L \propto A^H, \tag{3.2}$$

where H is now commonly called the Hack exponent (Rodriguez-Iturbe and Rinaldo, 1997). His analysis of basins over a wide range of areas (~1-1000 km^2) yielded an H value of 0.6. Montgomery and Dietrich (1992) expanded the analysis to include small unchannelized basins ($A < 1$ km^2) and very large basins ($A > 10^9$ km^2) and found that the structural relation between area and length had an exponent of 0.49. The theoretical study of Shreve (1967) also supports the notion that the Hack exponent is independent of basin area for $A < 10^3$ km^2. There are no previous studies, however, that examine the variability of the Hack exponent as a function of basin evolution.

The scale invariance of Hack's Law allows for rephrasing of Eq. 3.2 as the relationship between contributing area and distance from the divide x along an individual profile:

$$A \propto x^{1/H}. \tag{3.3}$$

As expressed in Eq. 3.3, the value of the Hack exponent relates the distance along a profile to the junction spacing and contributing area of tributary streams.

The Hack exponent is calculated by least-squares regression of the logarithms of

the distance-area data. To calculate the uncertainty of the best-fit exponent, it is necessary to assume that the data errors have the same standard deviation as the residuals of the regression (Press et al., 1998).

Figure 3.10 shows the best-fit values of H and 2σ uncertainties plotted versus transect distance. The correlation coefficients of all the regressions exceed 0.95. The values have a mean of 0.57 and range from 0.53 to 0.63. There is an increase in the Hack exponent from Basin 27 ($H = 0.55$) to Basin 22 ($H = 0.62$) but, north of Basin 22, the values range from 0.53 to 0.63 with no spatially coherent trend.

Profile Analysis

Knickpoints

The form of equilibrium river channels is thought to reflect a temporal balance between slope, discharge, sediment transport, and bed roughness (Knighton, 1998). The association between equilibrium channels and smooth profiles requires an additional assumption of uniform tectonic forcing and local conditions such as rock strength. Therefore, the existence of knickpoints, which are abrupt changes in profile elevation, is an important indicator of either temporal disequilibrium of a river profile or persistent nonuniformity of forcing or local conditions along a river profile.

I document the location and relief of ten knickpoints along eight ECR river profiles (Fig. 3.11). Gradual, yet significant, convexities and stretches of roughness in the profiles are common and an attempt was made to identify knickpoints as abrupt changes in profile elevation with more than 100 m of relief. This cutoff was used to avoid misinterpretation of possible artifacts created during the original construction of the DEM or those introduced by the sink filling algorithm in the DEM processing.

Knickpoints in the ECR profiles range in relief from 250 m to 600 m and in length from 0.6 km to 4.5 km. Individual knickpoints contribute 10%-40% of the total relief of the main channel. In Basins 13 and 15, which each have two knickpoints, the cumulative proportions are 25% and 30%, respectively.

To examine the correlation between knickpoint location and known lithologic contrasts, I overlay the map of knickpoint locations on the 1:500,000 geologic map (Ho, 1986) (Fig. 3.12). Knickpoint locations are approximated by circles of radius ~2.5 km.

Eight of ten knickpoints coincide with mapped lithologic boundaries (Fig. 3.12); the circle for the lower knickpoint on Profile 15 covers a small exposure of ultramafic rocks. The most prominent knickpoint, in Profile 9, does not correspond to any mapped change in lithology. A smaller knickpoint in Profile 19 apparently lies completely within a unit of greenschist-grade rocks.

Using the broad measures of age and metamorphic grade given by Ho (1986), I find that knickpoint location is not simply related to an upstream transition from younger and presumably weaker lithologies to older, stronger lithologies. In Basins 20 and 22, they occur at upstream transitions from Tertiary units to pre-Tertiary basement units while, in Basin 18, a knickpoint occurs at an upstream transition from a basement unit to a Tertiary unit. The knickpoint in Basin 2 occurs at an upstream transition from older to younger Tertiary units.

Slope-area analysis

The relationship between slope and contributing area along a river profile is an indicator of both the processes that erode the channel and the patterns of forcing parameters, such as precipitation and uplift (Montgomery and Foufoula-Georgiou, 1993; Willgoose, 1994; Rodriguez-Iturbe and Rinaldo, 1997; Whipple et al., 2000; Roe et al., 2002; Kirby and Whipple, 2001). In the absence of variable forcing, different process regimes have been identified from slope-area data (Fig. 3.13): (1) a hillslope regime ($A < 0.01 - 0.1$ km^2) where slope has a positive dependence on area, (2) a debris flow regime ($A < 1$ km^2) where slope has a weak negative dependence on area, and (3) a bedrock or mixed bedrock-alluvial channel regime ($A \gg 1$ km^2) where slope has a stronger negative dependence on area (Montgomery and Foufoula-Georgiou, 1993).

In active orogens, bedrock channels typically constitute a large portion (85-90%)

of the total profile relief (Whipple et al., 1999) and much work has been done to determine the appropriate functional form of the bedrock erosion law for mountain channels (Whipple and Tucker, 1999; Snyder et al., 2000; Whipple and Tucker, 2002; Tomkin et al., 2003). Most channels in Taiwan have a mixed bedrock-alluvial reach-scale morphology (i.e., mantles of gravel and boulders), but since there is no consensus over the functional form of the erosion law for such channels, I consider only the detachment-limited stream power law:

$$E = K p_o^m A^m S^n, \tag{3.4}$$

where K is the erodibility of the bedrock, p_o is the average precipitation rate, and m and n are process variables whose ratio is known as the intrinsic concavity θ (Whipple and Tucker, 1999). At steady state, with uniform uplift rate U, the slope-area relationship can be expressed as:

$$S = (U/K)^{1/n} p_o^{-\theta} A^{-\theta}. \tag{3.5}$$

Thus, for uniform uplift and rock strength, the steady state slope-area relationship is predicted to be a power law with a slope of $-\theta$ in log space.

Whipple and Tucker (1999) argued that the intrinsic concavity is limited to a narrow range of values (0.4-0.6). Deviation of observed concavities from this range is possible for either spatially variable uplift (Kirby and Whipple, 1999) and precipitation (Roe et al., 2002). Spatial gradients in uplift can account for a larger range (0.7-2.1) (Kirby and Whipple, 1999) than the orographic precipitation models of Roe et al. (2002), which, for an intrinsic concavity of 0.5, can account for a range of 0.4-0.6.

Extraction of river profiles from any DEM requires filling of local sinks, which produces flat segments that are particularly numerous in the lower portions of profiles. Because the Taiwan DEM was already filled when obtained, it is not possible to estimate the extent to which profile elevation has been altered by the filling process. I attempt to correct for filling by (i) removing all flat segments, (ii) connecting the

remaining data, and (iii) interpolating both the profile elevation and contributing area to an array of evenly spaced points (Δx=40m) that span the entire length of the original profile.

The slope of the elevation profile is calculated by a linear regression of the elevation-distance data within a moving window (Tomkin et al., 2003). I chose a width of 1 km because it is short relative to the total length of the profiles yet long enough to filter out most filling artifacts. I calculate the concavity of the channel segment ($A \gg 1$ km^2) by least-squares regression of the logarithms of the slope-area data. Uncertainties are estimated by the standard method given by Press et al. (1998).

The slope-area data from the ECR river profiles typically consist of the three segments shown schematically in Fig. 3.13. The transition interpreted to be between the debris flow and channel segments ranges from abrupt to gradual and is often completely obscured by noise in the slope data. Perturbations from a linear power-law slope-area relationship are ubiquitous, especially in the lower portion of the ECR profiles. In some instances, the noise is a record of knickpoints identifiable from the elevation profile (Fig. 3.14a) while in others it represents more subtle roughness (Fig. 3.14b).

Discerning smooth versus rough profiles is somewhat subjective. The smoothest set of profiles yield concavity values that are relatively invariant of the details of the analysis (e.g., small changes in the window length and in the bounds of the regression). Only these concavities are considered to be robust.

The best-fit concavities for the smooth ECR profiles are shown in Fig. 3.15. The values range from 0.6 in Basin 23 to 1.45 in Basin 7. As a group, the river profiles from Basins 23-27 are smoother and yield better fits than river profiles from the northern basins. The three highest values occur in small basins that do not extend to the main divide. There are not enough data in the central portion of the range to discern a spatial trend in the values.

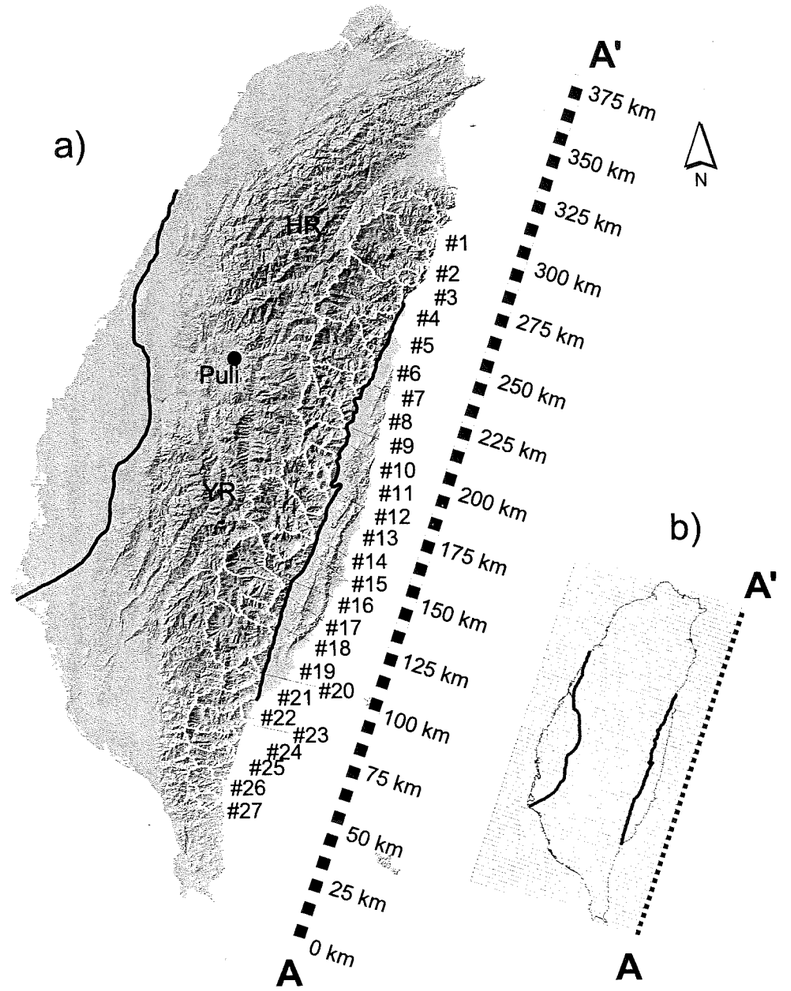

Figure 3.1: a) 40 meter Taiwan DEM with ECR basins and river profiles. HR: Hsüehshan Range, YR: Yushan Range. b) Volume, and mean and maximum elevation are calculated in 5 km wide swaths. Calculations are clipped at the eastern boundary of the Central Range and the western boundary of the Western Foothills (thick black line).

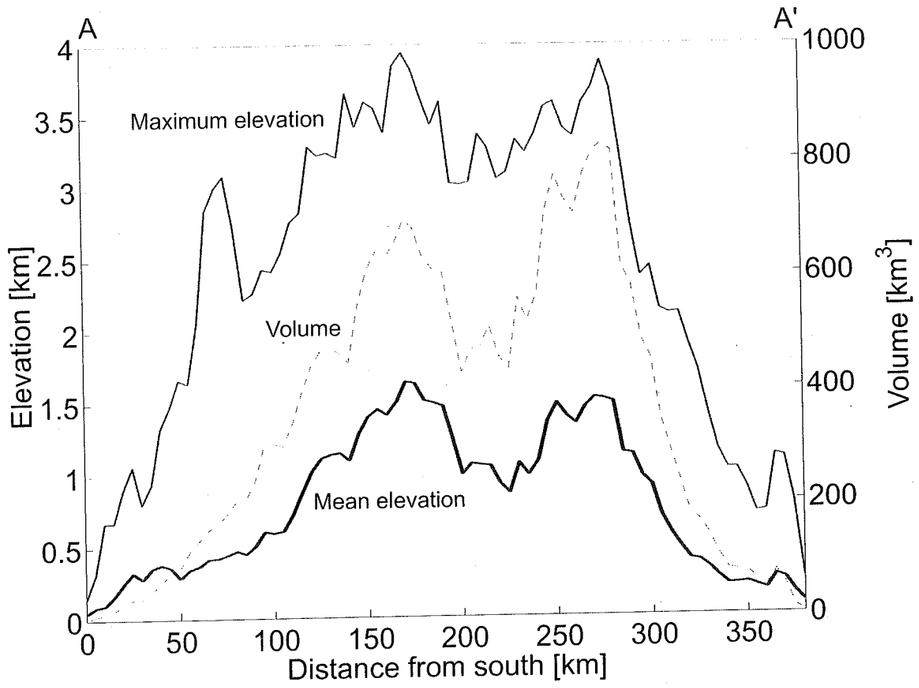

Figure 3.2: Volume, and mean and maximum elevation within cross-island swaths (Fig. 3.1b). From the south, all three quantities increase gradualy and attain constant values ~125 km north of the southern tip.

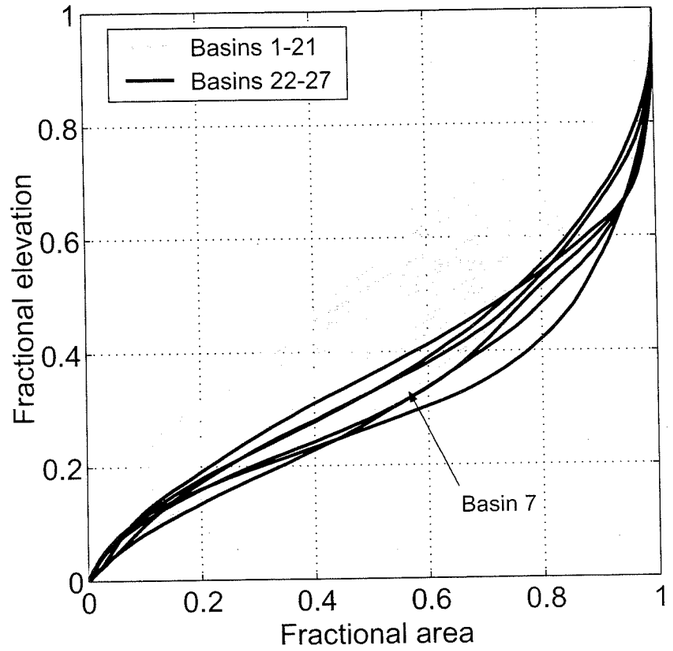

Figure 3.3: Hypsometric curves of ECR basins. Forms can be divided into two groups. Basins 22-27 have proportionately more area at lower relative elevations than do Basins 1-21. The most significant outlier in the northern population, Basin 7, has a form more similar to the southern population.

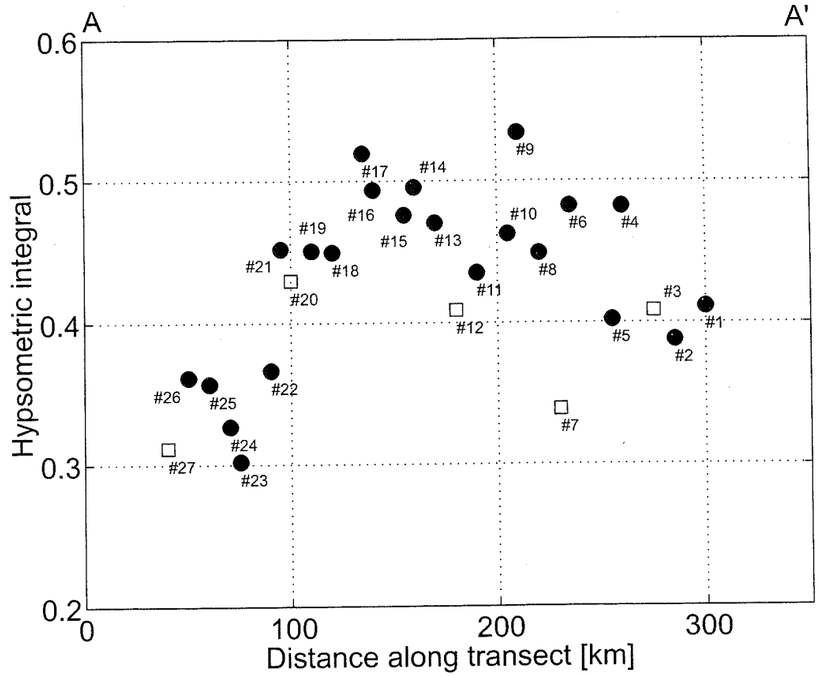

Figure 3.4: Hypsometric integral of ECR basins. There is a general northward increase in the hypsometic integral from Basin 27 to Basin 17. Small basins (A<100 km^2) marked with squares, larger basins with filled circles.

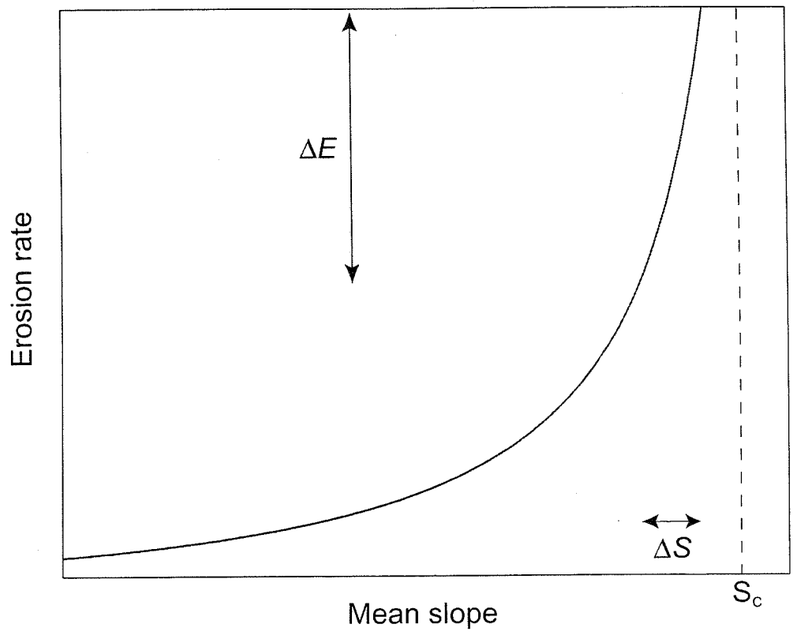

Figure 3.5: Functional form of $E \propto 1/(1-(\overline{S}/S_c)^2)$. Erosion rate approaches infinity as slope approaches the critical value S_c, which is set by the hillslope strength. Near the critical value, small changes in slope are able to accommodate large variations in erosion rate (gray region), thus mimicing threshold behavior.

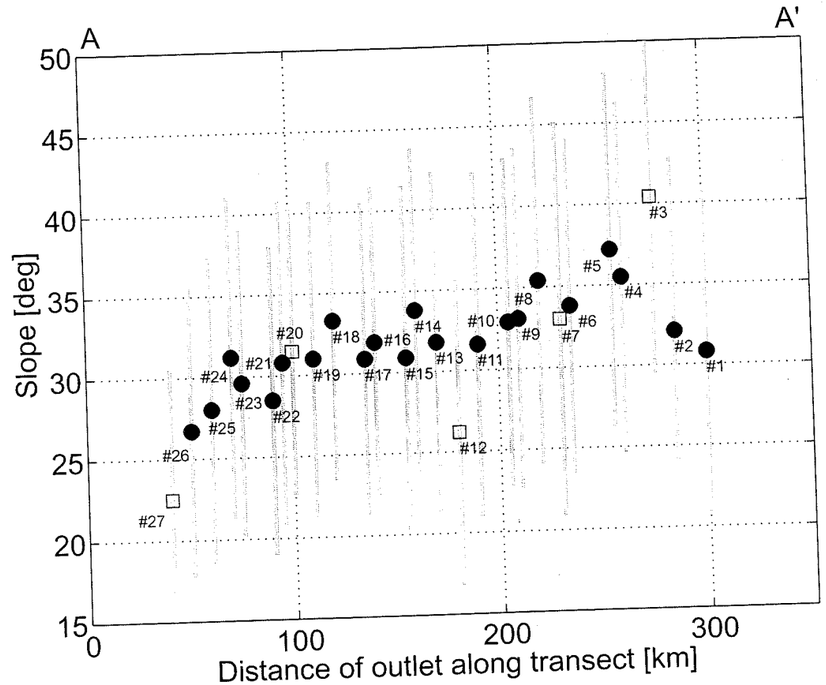

Figure 3.6: Mean and one standard deviation of local slope distributions of ECR basins. Mean slope increases from Basin 27 to Basin 21, remains relatively constant until Basin 10, and then increases to maximum in Basin 3. Small basins ($A < 100$ km^2) marked with squares, larger basins with filled circles.

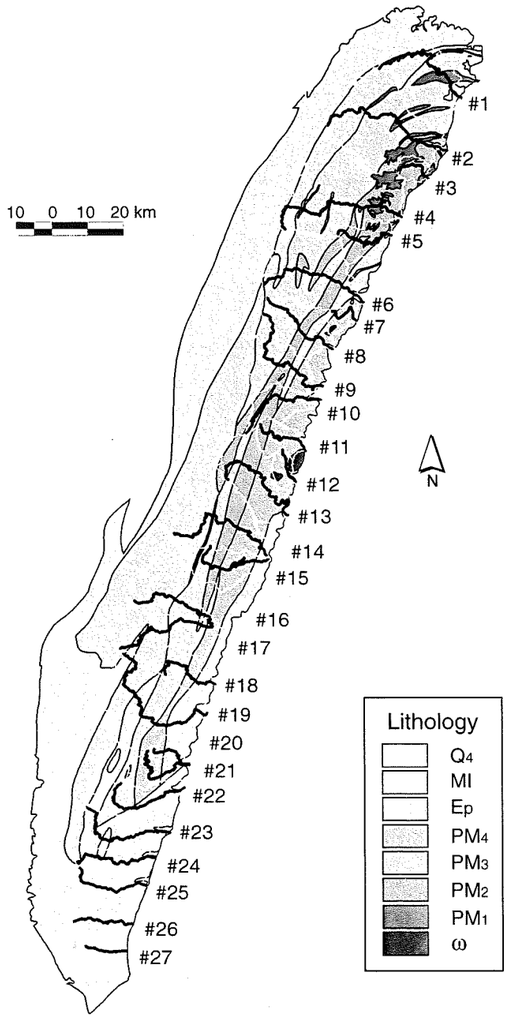

Figure 3.7: 1:500,000 geologic map of the ECR (Ho, 1986). Legend: Q4: Holocene alluvium; MI: Miocene argillites, slate, phyllite; Ep: Eocene slate, phyllite; PM4: Paleozoic-Mesozoic blackschist; PM3: Blackschist, greenschist, siliceous schist; PM2: Metamorphosed limestone; PM1: Gneisses and migmatite; ω: Mafic igneous rocks.

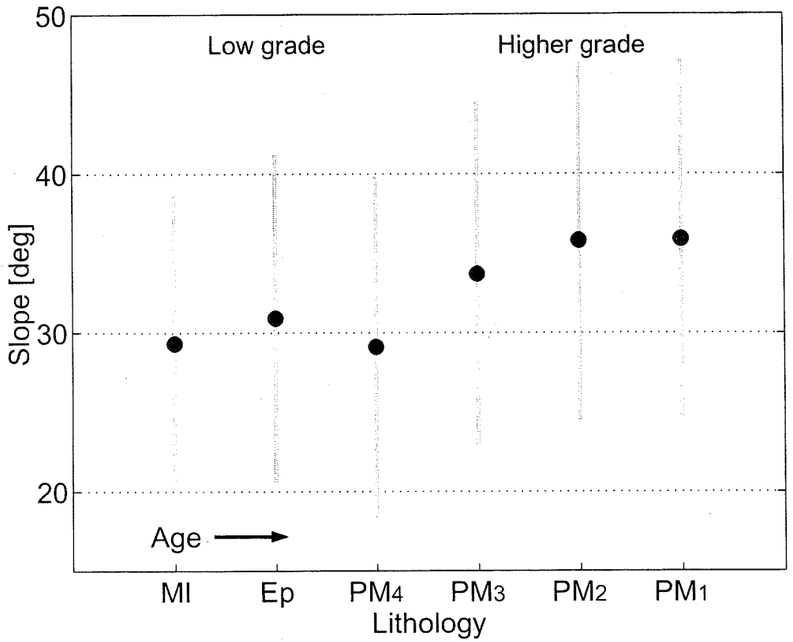

Figure 3.8: Mean and one standard deviation of slope distributions for lithologies within Basins 1-20. Higher-grade metamorphic rocks (PM1-PM3) have higher mean slopes than lower-grade rocks (PM4, Ep, MI). Legend: MI: Miocene argillites, slate, phyllite; Ep: Eocene slate, phyllite; PM4: Paleozoic-Mesozoic blackschist; PM3: Blackschist, greenschist, siliceous schist; PM2: Metamorphosed limestone; PM1: Gneisses and migmatite.

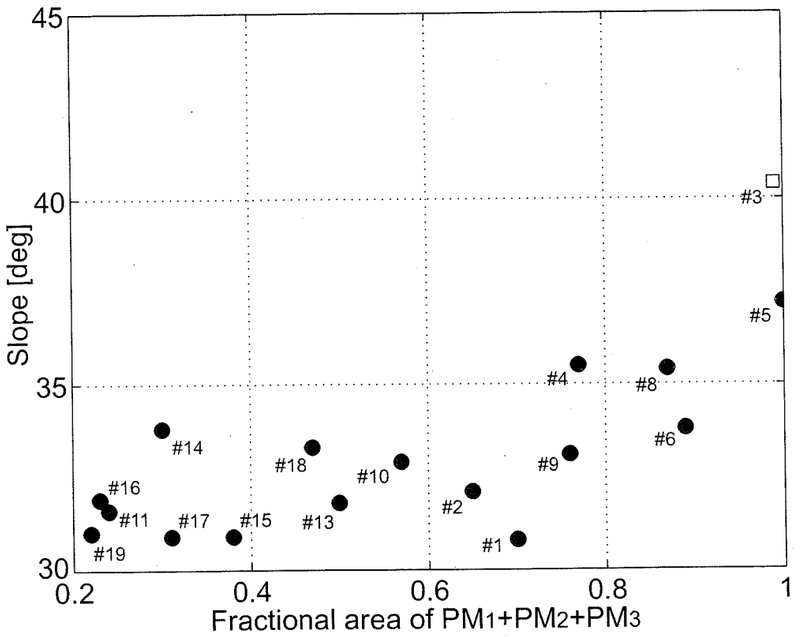

Figure 3.9: Dependence of mean basin slope on portion of basin within three most resistant lithologies. There is a positive correlation between slope and lithology for fractional areas >75% and no relationship for fractional areas below 75%. Small basins ($A < 100$ km^2) marked with squares, larger basins with filled circles.

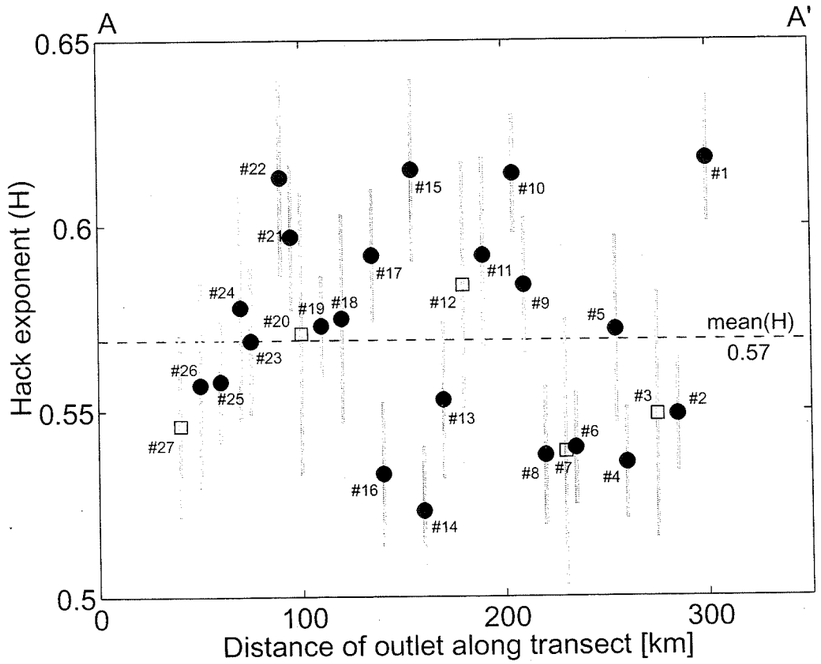

Figure 3.10: Hack exponent and 2σ uncertainty for ECR basins. Linear regression of the Hack exponent values for Basins 1-20 yields a slope of -0.02 and a correlation coefficient of 0.01. Small basins ($A < 100$ km^2) marked with squares, larger basins with filled circles.

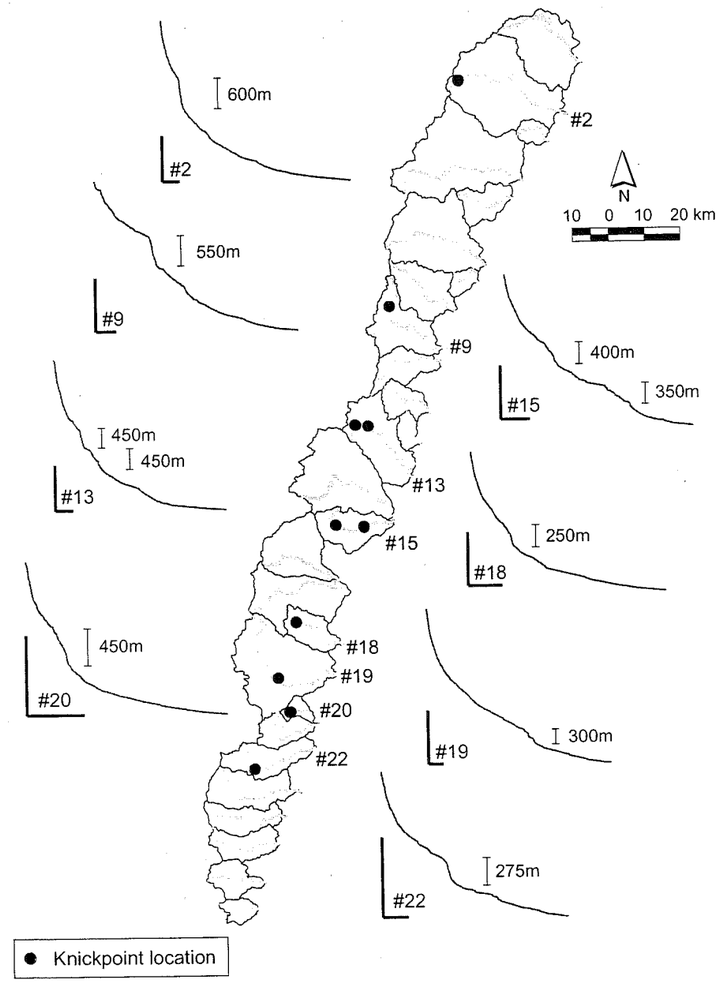

Figure 3.11: Documented knickpoints along ECR profiles with greater than 100 m of relief. Horizontal and vertical scales for each profile are 5 km and 1 km, respectively. Knickpoints contribute 10-40% of the total profile relief.

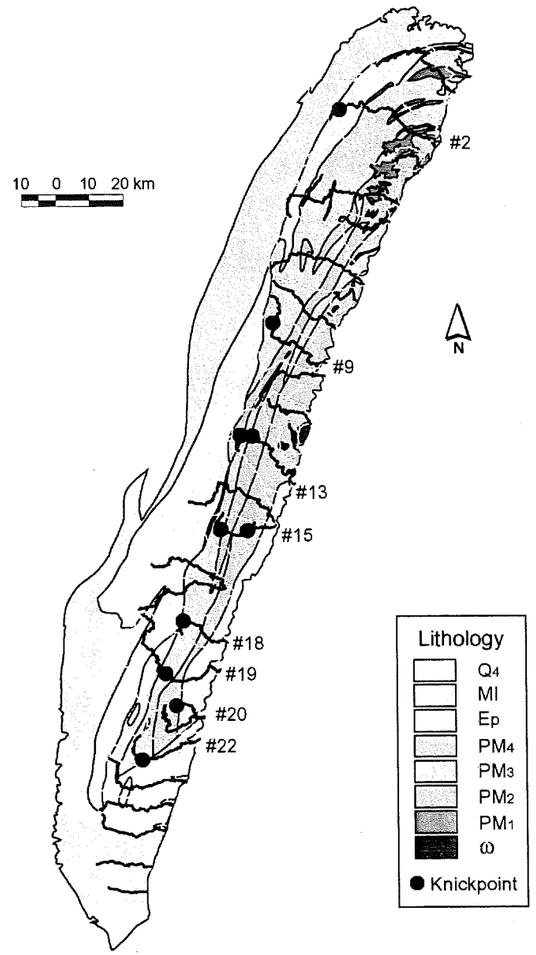

Figure 3.12: Coincidence of knickpoint location with lithologic contacts mapped at 1:500,000 scale (Ho, 1986). Knickpoint locations are approximated by circles of radii 2.5 km. Legend: Q4: Holocene alluvium; MI: Miocene argillites, slate, phyllite; Ep: Eocene slate, phyllite; PM4: Paleozoic-Mesozoic blackschist; PM3: Blackschist, greenschist, siliceous schist; PM2: Metamorphosed limestone; PM1: Gneisses and migmatite; ω: Mafic igneous rocks.

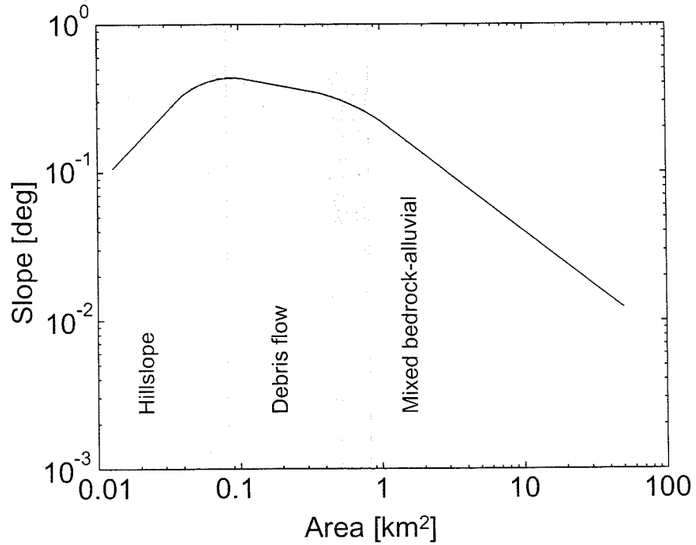

Figure 3.13: Schematic illustration of expected slope–area relationships for hillslope, debris flow, and channel regimes (Montgomery and Foufoula-Georgiou, 1993).

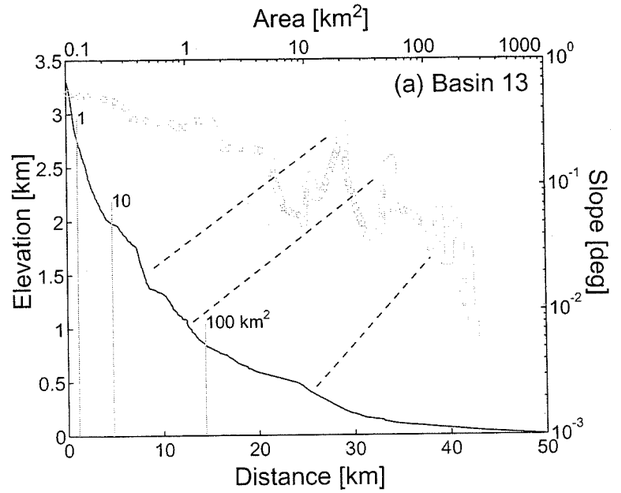

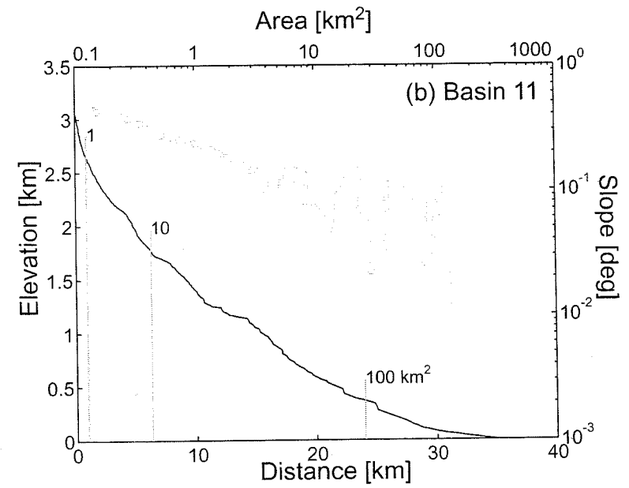

Figure 3.14: Examples of variability in slope–area data caused by (a) observed knickpoints and (b) more subtle roughness. This roughness precludes calculation of a concavity value.

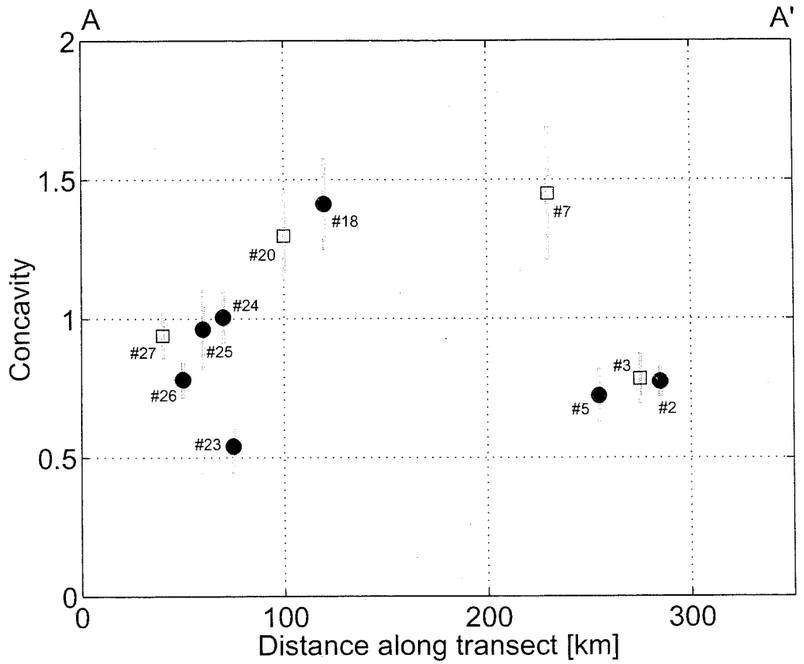

Figure 3.15: Best-fit concavities and 2σ standard deviations for smooth profiles. The three highest values are found in small basins that do not reach the main drainage divide. Small basins ($A < 100$ km^2) marked with squares, larger basins with filled circles.

Chapter 4

DISCUSSION

Swath profile analysis

The swath profile analysis shows that the volume, mean elevation, and maximum elevation increase from the southern tip of the island and reach constant values ~125 km northward (Fig. 3.2). From 125 to 275 km north, there is a 100 km wavelength oscillation in all three quantities.

The swath profile data indicate that the island has a roughly constant size from 125 km N to 275 km N and that growth to this form occurs gradually from the southern tip of the island. I interpret the form to be a measure of the balance between tectonic and erosional forcing. Assuming that the propagation rate has been steady, I use the space-time equivalence to infer that the growth to a steady form represents the attainment of a large-scale topographic SS in Taiwan. Using the range of propagation rates (55-90 mm/yr), the time to SS is 1.4-2.3 Myr after subaerial exposure. I prefer the upper estimate because the propagation rate was determined using a more accurate representation of the collision obliquity (Byrne and Liu, 2002).

The scale and amplitude of the noise level in the inferred SS are significant. At the 100 km length scale, the maximum amplitude of the noise level is 20% of the SS. This variability could represent either disequilibrium or nonuniform conditions; in the Hsüehshan Range, it reflects large-scale structure.

Basin analyses

Hypsometry

Two distinct, spatially-correlated populations exist within the hypsometric curve data (Fig. 3.3). Basins 22-27 have more relative area at lower relative elevations than do Basins 1-20. The increase of the hypsometric integral from the southernmost basins to basins ~120-130 km northward suggests that the transition in hypsometry might be more gradual than suggested by the hypsometric curves (Fig. 3.4).

The transition in hypsometric curve form occurs 95 km north of the southern tip of the island. This coincides within 30 km of the transition from pre-SS to SS topography inferred from the swath profile data. I interpret this coincidence as evidence that basin hypsometry records the pre-SS to SS transition.

The manner in which the hypsometric curves change, however, is the inverse of the predictions of Strahler (1964) and Willgoose and Hancock (1998). The predictions of Willgoose and Hancock (1998) were based on a model that considered the uplift of an initially flat basin of fixed size with respect to a fixed baselevel (Fig. 4.1a). In that model, incision initiates at the outlet and gradually propagates into the basin (Fig. 4.1b,c). The unincised portion of the basin remains at the maximum elevation, effectively acting like a plateau. Thus, the change in hypsometry shown in (Fig. 4.1d) is controlled by the gradual destruction of a plateau at a high relative elevation. In contrast, the subaerial width of Taiwan has increased with continued emergence, which has resulted in continuous incision close to the divide of all of the pre-SS basins.

Within the northern population of hypsometric curves, the most significant outlier is Basin 7, a small basin ($A = 50$ km^2) that borders the deformation front. The DEM of Basin 7 (Fig. 4.2) shows that, from the headwaters, the main channel flows ESE until it turns sharply to the NE. The lower segment is bounded to the east by a low ridge, which separates it from the Longitudinal Valley. The existence of the lower valley results in a disproportionately large amount of area at low relative elevations and, thus, a hypsometric curve more similar to those found in the southern basins.

Strahler (1964) argued that measurements of hypsometry could differentiate young or pre-SS topography from mature or SS topography. The results of the ECR basin analysis demonstrate that young topography might have different hypsometries depending on the conditions under which landscape evolution occurs. This suggests that recognition of topographic SS requires a comparison of basin hypsometries rather than identification of distinct young and mature hypsometric forms.

Slope distributions

From the southernmost basin, mean basin slope increases until it attains a constant value ($31^o \pm 2^o$) between 100 and 200 km north of the southern tip of the island (Fig. 3.6). Basin slope then increases from 33^o in Basin 9 to 41^o in Basin 3. Within Basins 1-20, there is a correlation between basin slope and the exposure of higher-grade metamorphic units, which have higher mean slopes than do lower-grade units. Basins with greater than 75% of the highest grade metamorphic units (PM1, PM2, and PM3) have the highest mean slopes in the ECR.

The transition to a relatively constant mean slope (Fig. 3.6) is within ~25 km of the transition from pre-SS to SS topography inferred from the swath profile data. In the context of the non-linear erosion model (Eq. 3.1 and Fig. 3.5), I interpret this as evidence for a hillslope response to differences in erosion rate between pre-SS and SS topography. The behavior of the mean slope within the SS basins also matches the predictions of the erosion model. Here, the mean slope is related to the distribution of resistant lithologies, which is analogous to a lithologic control of the value of S_c in Eq. 3.1. Fig. 4.3 shows a summary illustration of the evolution of topography from pre-SS, where gradients in erosion rate are reflected by differences in mean slope, to SS, where the value of the mean slope is determined by strength of hillslopes.

An alternative interpretation of the slope data in Fig. 3.6 is that all spatial correlation in the data actually reflects the distribution of metamorphic grade. Thus, the lower slopes in the south coincide with the presumably weaker Tertiary units (MI and Ep) and the higher slopes in the central and northern ECR coincide with greater

exposure of the pre-Tertiary units. This implies that hillslopes in all basins have attained a threshold slope. The northward trend of increasing mean slope from Basin 27 to Basin 23, however, occurs almost entirely within the Tertiary MI unit, which indicates that the trend is independent of lithology.

Hack's Law

The value of the Hack exponent increases from 0.54 in Basin 27 to 0.62 in Basin 22 but, north of Basin 22, it varies from 0.53 to 0.63 with no spatially coherent trend. The mean of the exponent from all the ECR basins is 0.57.

Within the SS region (Basins 1-21), there is no consistency in the value of the Hack exponent that would suggest that a single, steady value is attained. That the range of observed values exceeds the the size of the average 95% confidence interval suggests that there are real, albeit small, differences in the network architecture of the ECR basins. Because values from pre-SS basins are similar to values from SS basins, the Hack exponent appears to be set early on in basin evolution.

Between major tributary junctions, the residuals of the regressions to the distance-area data are strongly correlated (Fig. 4.4). This is due to the stair-step nature of the area data, where each step corresponds to a tributary junction. In between these junctions, the slope of the data is much lower, representing the lower rate of area addition by hillslopes. Hack's Law, therefore, is not a good description of the area-distance relationship on scales much smaller than the entire profile length.

Profile analyses

Knickpoints

Ten knickpoints with relief greater than 100 m exist in the ECR. The proportion of the total profile relief contributed by the knickpoints ranges from 10% to 40%. Eight of the ten knickpoints coincide with mapped lithologic boundaries. I infer, based on a broad classification of metamorphic grade (Ho, 1986), that the knickpoints do not

simply correspond to upstream transitions from weaker to stronger rocks.

There are two possible mechanisms for the formation of the ECR knickpoints: transient perturbations in the profile and stationary nonuniformity of forcing along a profile. Knickpoints that are created by vertical displacement of a profile relative to its baselevel (e.g., sea level drop, rupture by an earthquake) meet one of two fates: (i) propagation through the entire channel network or (ii) propagation until stalling at an upstream increase in rock strength. The large relief of the documented knickpoints in the ECR suggests that they are not each the result of one event.

From this, I infer that the coincidence of knickpoint location and lithologic contacts is a result of stationary spatial gradients in rock uplift rate or rock strength. This non-uniformity could be either a step-function increase or a spike. If a river profile is at SS and experiences an increase in uplift rate in the upstream portion (i.e., a step-function increase), a knickpoint will form if the upstream profile can not keep pace with the new uplift rate. There are several possible outcomes, all of which are non-steady: (i) the knickpoint will propagate upstream, (ii) the profile above the knickpoint will gradually steepen, or (iii) if the knickpoint region is very resistant to erosion, it will not propagate and will increase in relief over time. In contrast, a spike in uplift rate or rock strength results in stationary knickpoints with steady relief. This is because the profile steepens until it achieves a steady form in which erosion balances the uplift rate. I prefer the mechanisms that predict that the knickpoints are stationary. It is not possible, however, to determine whether they are steady.

Knickpoints contribute up to 40% of the total profile relief of some ECR river profiles. Because expressions of non-uniformity are so significant in many ECR profiles, understanding the response of knickpoints to stimuli such as changes in climate or background uplift rate is important to understanding the integrated response of the ECR river profiles.

Slope-area analysis

The slope-area analysis indicates a wide range of concavity values (0.55-1.45), with the highest values far outside the range of predicted intrinsic concavities (Tucker and Whipple, 1999). Roughness in most central ECR profiles precludes regression of the slope-area data. Consequently, there are not enough data to determine if there is a spatial trend in the concavity values.

The slope-area data and elevation profiles of the three profiles (profiles 7, 18, and 20) with concavities greater than 1.0 are shown in Fig. 4.5. In profiles 18 and 20, the high concavity segments occur downstream of knickpoints discussed in the previous section (Fig. 3.11). The high concavities are not artifacts of the method used to calculate slope because the segments do not include points less than 0.5 km downstream of the knickpoint.

A possible explanation is that the high concavities are a result of the same process that sets the location of the knickpoints. Kirby and Whipple (1999) argued that, in the Siwalik foothills of the Himalaya, high observed concavities (0.7-2.1) were the result of downstream decreases in uplift rate. Presumably, downstream decreases in rock strength could also mimic this behavior. For instance, if the knickpoints represent regions of high uplift, the high concavities could indicate that the decrease in uplift rate away from the knickpoint is gradual, rather than abrupt.

The high concavity section of Basin 7 occurs completely downstream of the abrupt change in the direction of the main channel (Fig. 4.2). This study is not able to resolve whether this coincidence is related to the cause of the high concavity value.

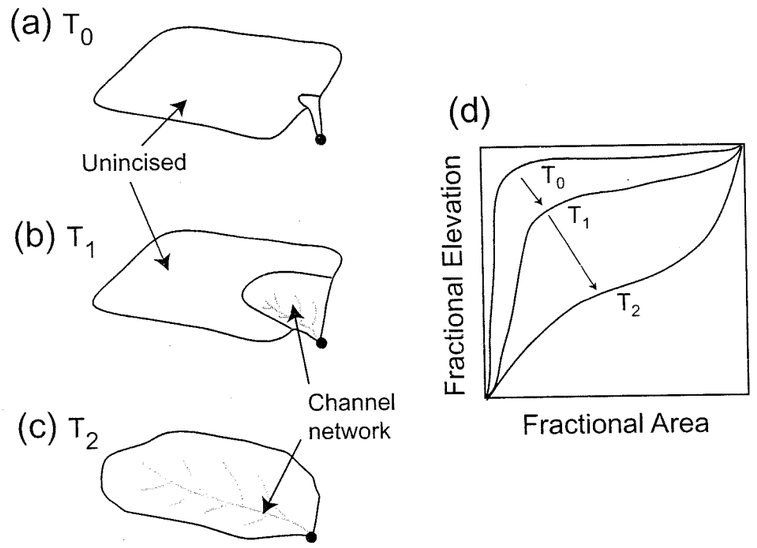

Figure 4.1: Schematic illustration of the evolution of basin hypsometry according to the model of Willgoose and Hancock (1998). Basin evolution begins with initial uplift of the interior of the basin relative to a fixed base level. The hypsometric curve at T_0 in panel (d) reflects that most of the area of the basin is at the maximum elevation. Over time, incision propagates into the basin (panel (b)), decreasing the amount of area at the maximum elevation. At the equilibrium state (panel (c)), elevation is distributed more evenly.

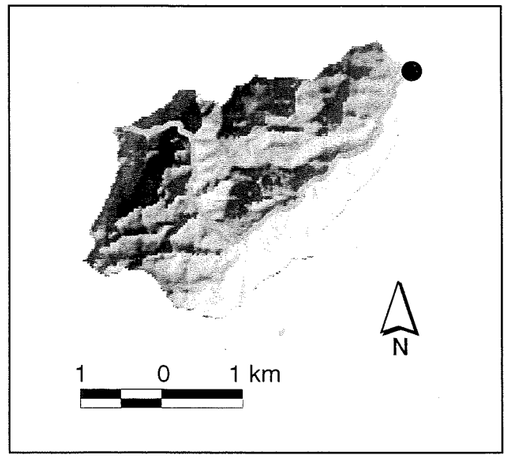

Figure 4.2: DEM of Basin 7. Abrupt change in direction of main channel occurs upstream of the lower valley that causes anomalous hypsometric curve. Outlet denoted by filled circle in northeastern corner of basin.

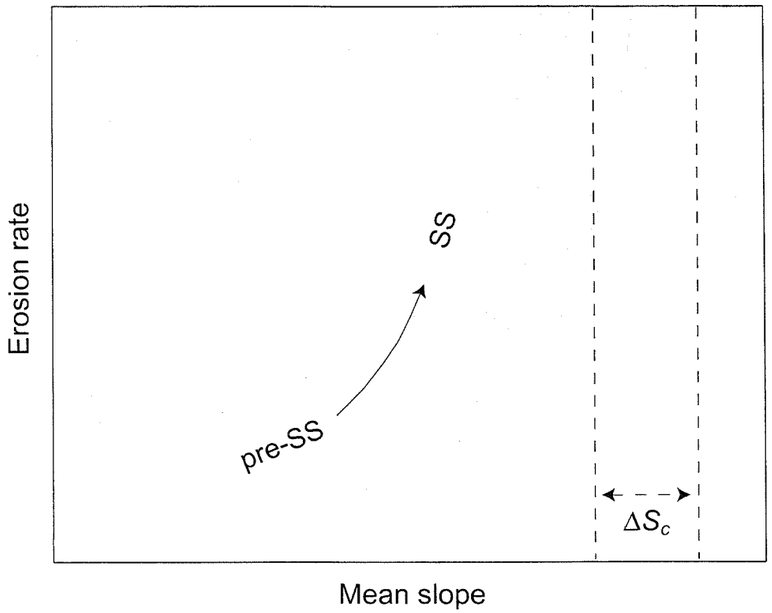

Figure 4.3: Schematic illustration of the evolution of topography from pre-SS to SS following the erosion rate-slope relationship posited by Montgomery and Brandon (2003). In pre-SS topography, there is a near-linear relationship, such that differences in erosion rate are expressed by differences in mean slope. In SS topography, mean slope is independent of erosion rate and is strongly influenced by the critical slope value S_c.

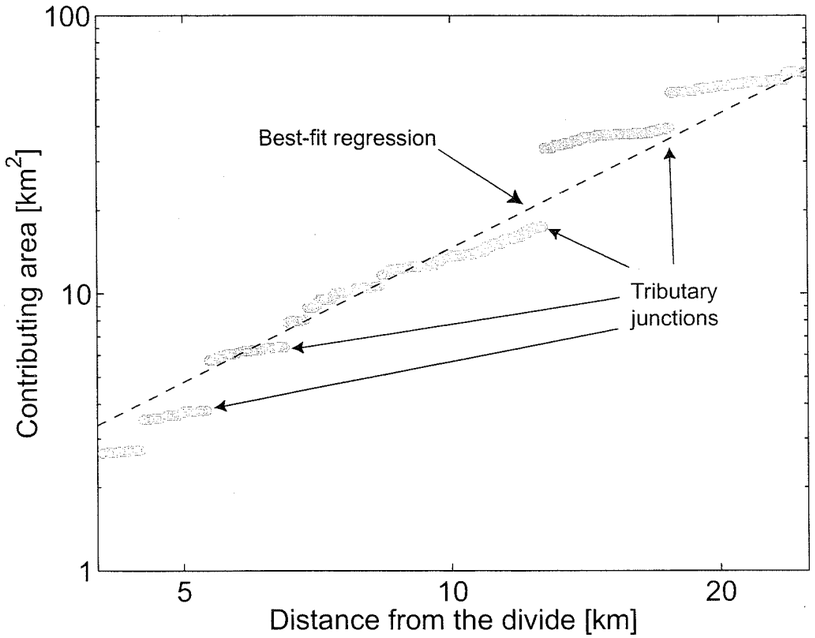

Figure 4.4: Portion of the area-distance data from Basin 1 with best-fit regression line. Jumps in contributing area correspond to major tributary junctions. In between these junctions, area increases slowly from gradual contribution of hillslopes. At this scale, Hack's Law is not a precise description of the area-distance relationship.

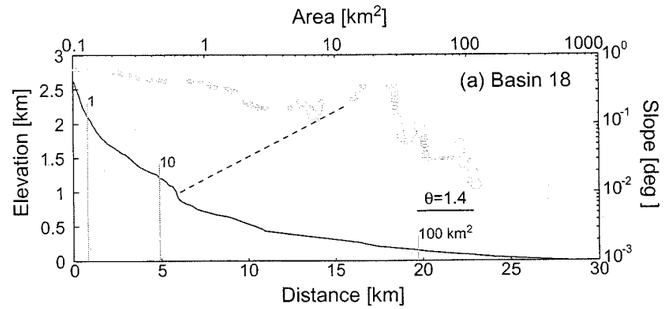

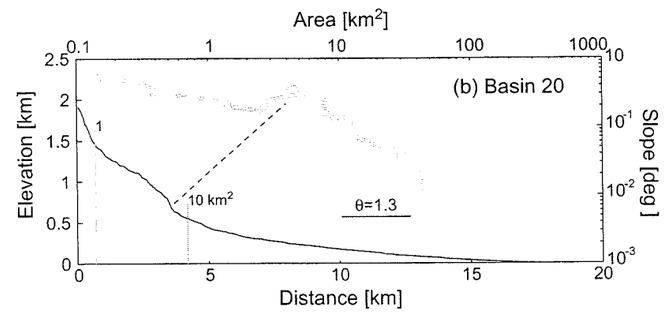

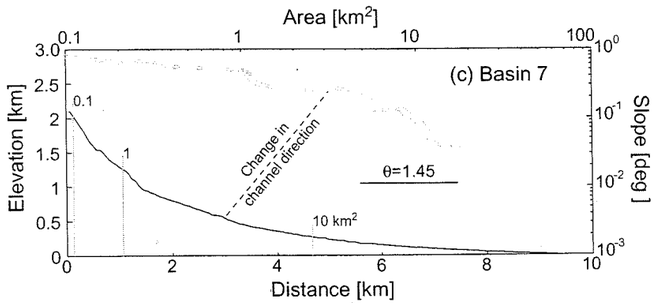

Figure 4.5: Elevation profiles and slope–area data for profiles with concavities greater than 1.0. High concavity values of Profiles 18 and 20 are related to conditions downstream of major knickpoints. The high concavity value of Profile 7 is coincident with an abrupt change in the direction of the main channel (see Fig. 4.2).

Chapter 5

SUMMARY AND CONCLUSIONS

Topographic steady state in Taiwan is expressed by the existence and coincidence of transitions in several characteristics of the topography. The volume, mean elevation, and maximum elevation of the cross-island swaths all increase northwards from the southern tip of the island for 125 km, further north they maintain roughly constant values for 250 km. I interpret the growth to a steady form as evidence that Taiwan has reached a large-scale topographic SS. Given that the collision between the Eurasian continental margin and Luzon Arc has propagated southwards at a rate of 55-90 mm/yr, I use the space-time equivalence to estimate that SS is achieved 1.4-2.3 Myr after emergence above sea level.

A northward increase to a steady value is also observed in the mean local slope of the ECR basins. Mean local slope increases from 23^o in the southernmost basin and reaches a near constant value of 31^o at 95 km north of the southern tip of the island. The association between this trend and the pre-SS to SS transition is not completely unambiguous because this study can not dismiss the hypothesis that the trend in the slope data is a result of the distribution of lithology. There is a similar trend in the hypsometric integral of the ECR basins. The hypsometric integral increases from $\sim$0.33 in the southernmost basins to $\sim$0.48 at 125-225 km north of the southern tip of the island. Though the transition in hypsometry coincides with the inferred pre-SS to SS transition, the form of the hypsometric curve changes in a sense opposite of previous predictions. Because of the complications in interpreting the basin slope and hypsometry data, recognition of SS based solely on these two analyses would be difficult.

Neither the Hack exponent or the form of ECR river profiles appears to record

the transition to topographic SS. The similarity of the Hack exponent between pre-SS and SS basins suggests that it is set early on in basin evolution. River profile form is not a good indicator of SS because of its sensitivity to local gradients in rock uplift.

All of the analyses indicate that significant variability can exist in a landscape that is in a large-scale SS. Moreover, at the broadest scale (~100 km), variability with an amplitude of 20% of the SS can be attributed to large-scale structure. (e.g., uplift of the Hsüehshan Range). The mean local slope of basins in the SS portion of the ECR varies from 31° to 41°, with the first order control being the distribution of resistant lithologies. Within the SS basins, the Hack exponent ranges from 0.53 to 0.63 with no discernible spatial trend. Knickpoints, which are most likely the result of non-uniformity in the rock uplift field, vary in relief from 300 m to 600 m. Profile concavities varies from 0.45 to 1.45, with the highest values possibly a result of spatial variability in uplift rate.

In conclusion, topographic SS is apparent from broad spatial patterns in the cross-island form, hypsometry, and mean local slope. Variability in the topography of Taiwan would preclude the recognition of SS by smaller-scale studies. Finally, SS is best resolved by comparison of topographic properties along an age gradient, rather than identification of characteristic pre-SS and SS forms.

BIBLIOGRAPHY

Adams, J. (1980). Contemporary uplift and erosion of the Southern Alps, New Zealand. *Geological Society of America Bulletin*, 91:1–114.

Ahnert, F. (1970). Functional relationships between denudation, relief, and uplift in large mid-latitude drainage basins. *American Journal of Science*, 268:243–263.

Brandon, M. T., Roden-Tice, M. K., and Garver, J. I. (1998). Late Cenozoic exhumation of the Cascadia accretionary wedge in the Olympic Mountains, northwest Washington State. *Geological Society of America Bulletin*, 110:985–1009.

Brocklehurst, S. H. and Whipple, K. X. (2001). Glacial erosion and relief production in the Eastern Sierra Nevada, California. *Geomorphology*, 42:1–24.

Burbank, D. W., J., L., Fielding, E., Anderson, R. S., Brozovic, N., Reid, M. R., and Duncan, C. (1996). Bedrock incision, rock uplift and threshold hillslopes in the northwestern Himalayas. *Nature*, 379:505–510.

Byrne, T. B. and Liu, C.-S. (2002). Preface: Introduction to the geology and geophysics of Taiwan. In *Geology and geophysics of an arc-continent collision, Taiwan.* Geological Society of America.

Clark, M. B., Fisher, D. M., Lu, C.-Y., and Chen, C.-H. (1993). Kinematic analyses of the Hsuehshan Range, Taiwan: A large-scale pop-up structure. *Tectonics*, 12:205–217.

Gilbert, G. K. (1877). *Report on the geology of the Henry Moutains (Utah).* Publication of the Powell Survey.

Hack, J. T. (1957). Studies on longitudinal profiles in Virginia and Marlyand. *United State Geological Survey Professional Paper*, 294.

Ho, C.-S. (1986). Geologic map of Taiwan.

Howard, A. D. (1994). A detachment-limited model of drainage basin evolution. *Water Resources Research*, 99:13,791–13,986.

Kirby, E. and Whipple, K. (2001). Quantifying differential rock-uplift rates via stream profile analysis. *Geology*, 29:415–418.

Knighton, D. (1998). *Fluvial forms and processes: A new perspective.* Edward Arnold, page 383.

Kooi, H. and Beaumont, C. (1996). Large-scale geomorphology: Classical concepts reconciled and integrated with contemporary ideas via a surface process model. *Journal of Geophyscial Research*, 102:3361–3386.

Koons, P. O. (1989). The topographic evolution of collisional mountain belts: A numerical look at the Southern Alps, New Zealand. *American Journal of Science*, 289:1041–1069.

Lee, J.-C., Angelier, J., Chu, H.-T., Hu, J.-C., and Jeng, F.-S. (2001). Continous monitoring of an active fault in a plate suture zone: a creepmeter study of the Chihshang Fault, eastern Taiwan. *Tectonophysics*, 333:219–240.

Lee, T.-Q., Kissel, C., Barrier, E., Laj, C., and Chi, W.-R. (1991). Paleomagnetic evidence for a diachronic clockwise rotation of the Coastal Range, eastern Taiwan. *Earth and Planetary Science Letters*, 104:245–257.

Montgomery, D. R., Balco, G., and Willett, S. D. (2001). Climate, tectonics and the mega-morphology of the Andes. *Geology*, 29:579–582.

Montgomery, D. R. and Brandon, M. T. (2002). Topographic controls on erosion rates in tectonically active mountain ranges. *Earth and Planetary Science Letters*, 201:481–489.

Montgomery, D. R. and Dietrich, W. E. (1992). Channel initiation and the problem of landscape scale. *Science*, 255:826–830.

Montgomery, D. R. and Foufoula-Georgiou, E. (1993). Channel network source representation using digital elevation models. *Water Resources Research*, 29:3925–3934.

Mouthereau, F., Lacombe, O., Deffontaines, B., Angelier, J., and Brusset, S. (2001). Deformation history of the southwestern Taiwan foreland thrust belt: insights from tectono-sedimentary analyses and balanced cross-sections. *Tectonophysics*, 333:293–322.

Penck, W. (1953). *Morphological analysis of land forms.* Macmillan, page 429.

Press, W. H., Teukolsky, S. A., Vetterling, W. T., and Flannery, B. P. (1998). *Numerical recipes in FORTRAN.* Cambridge University Press, page 963.

Rodriguez-Iturbe, I. and Rinaldo, A. (1997). *Fractal river basins: chance and self-organization.* Cambridge University Press, page 574.

Roe, G. H., Montgomery, D. R., and Hallet, B. (2002). Effects of orographic precipitation variations on the concavity of steady-state river profiles. *Geology*, 30:143–146.

Roering, J. J., Kirchner, E. E., and Dietrich, W. E. (1999). Evidence for nonlinear, diffusive sediment transport on hillslopes and implications for landscape morphology. *Water Resources Research*, 35:853–870.

Schmidt, K. M. and Montgomery, D. R. (1995). Limits to relief. *Science*, 270:617–620.

Shreve, R. L. (1967). Infinite topologically random channel networks. *Journal of Geology*, 77:397–414.

Snyder, N. P., Whipple, K. X., Tucker, G. E., and Merritts, D. J. (2000). Landscape response to tectonic forcing: Digital elevation model analysis of stream profiles in the Mendocino triple junction region, northern California. *Geological Society of America Bulletin*, 112:1250–1263.

Steno, T. (1977). The instantaneous rotation vector of the Philippine Sea Plate relative to the Eurasian Plate. *Tectonophysics*, 42:209–226.

Strahler, A. N. (1964). *Quantitative geomorphology of drainage basins and channel networks*, pages 4:39–4:76. McGraw Hill.

Suppe, J. (1981). Mechanics of mountain building and metamorphism in Taiwan. *Memoir of the Geological Society of China*, 4:67–89.

Teng, L. S. (1987). Stratigraphic records of the late Cenozoic Penglai orogeny of Taiwan,. *Acta Geology Taiwan*, 25:205–224.

Teng, L. S. (1996). Geology. *Extensional collapse of the northern Taiwan mountain belt*, 24:949–952.

Tomkin, J. H., Brandon, M. T., Pazzaglia, F. J., Barbour, J. R., and Willett, S. D. (2003). Quantitative testing of bedrock incision models for the Clearwater River, NW Washington State. *Journal of Geophyscial Research*.

Whipple, K. X., Hancock, G. S., and Anderson, R. S. (2000). River incision into bedrock: Mechanics and relative efficacy of plucking, abrasion, and cavitation. *Geological Society of America Bulletin*, pages 490–503.

Whipple, K. X., Kirby, E., and Brocklehurst, S. H. (1999). Geomorphic limits to climate-induced increases in topographic relief. *Nature*, 401:39–43.

Whipple, K. X. and Tucker, G. E. (1999). Dynamics of the stream-power river incision model: implications for height limits of mountain ranges. *Journal of Geophyscial Research*, 104:17,661–17,674.

Whipple, K. X. and Tucker, G. E. (2002). Implications of sediment-flux dependent river incision models for landscape evolution. *Journal of Geophyscial Research*, 107.

Willett, S. D. Slingerland, R. and Hovius, N. (2001). Uplift, shortening, and steady state topography in active mountain belts. *American Journal of Science*, 301:455–485.

Willett, S. D. and Brandon, M. B. (2002). On steady states in mountain belts. *Geology*, 30:175–178.

Willgoose, G. and Hancock, G. (1998). Revisiting the hypsometric curve as an indicator of form and process in transport-limited catchment. *Earth Surface Processes and Landforms*, 23:611–623.

Willgoose, G. R. (1994). A statistic for testing the elevation characteristics of landscape simulation models. *Journal of Geophyscial Research*, 99:13,987–13996.

Yu, S.-B., Chen, H.-Y., and Kuo, L.-C. (1997). Velocity field of GPS stations in the Taiwan area. *Tectonophysics*, 274:41–59.